Measurements relating fire radiative energy density and surface fuel consumption—RxCADRE 2011 and 2012

Journal:	*International Journal of Wildland Fire*
Manuscript ID:	Draft
Manuscript Type:	Research Paper
Date Submitted by the Author:	n/a
Complete List of Authors:	Hudak, Andrew; USDA Forest Service, Rocky Mountain Research Station Dickinson, Matthew; USDA Forest Service, Northern Research Station Bright, Benjamin; USDA Forest Service, Rocky Mountain Research Station Kremens, Robert; Rochester Inst of Technology, Center for Imaging Science Loudermilk, Eva (Louise); USDA Forest Service, Center for Forest Disturbance Science OBrien, Joseph; US Forest Service, Center for Forest Disturbance Science Hornsby, Benjamin; US Forest Service, Center for Forest Disturbance Science Ottmar, Roger; USDA Forest Service, Pacific Northwest Research Station
Keyword:	Remote sensing, Fuel, Scale: local

Surface fuel and fire radiative energy measures

Measurements relating fire radiative energy density and surface fuel consumption—RxCADRE 2011 and 2012

Andrew T. Hudak[A,F], *Matthew B. Dickinson*[B], *Benjamin C. Bright*[A], *Robert L. Kremens*[C], *E. Louise Loudermilk*[D], *Joseph J. O'Brien*[D], *Benjamin S. Hornsby*[D], *and Roger D. Ottmar*[E]

[A]USDA Forest Service Rocky Mountain Research Station, Forestry Sciences Laboratory, 1221 South Main Street, Moscow, ID 83843, USA

[B]USDA Forest Service, Northern Research Station, 359 Main Road, Delaware, OH 43015, USA

[C]Rochester Institute of Technology, Center for Imaging Science, 54 Lomb Memorial Drive, Rochester, NY 14623, USA

[D]USDA Forest Service, Southern Research Station, Center for Forest Disturbance Science, 320 Green St., Athens, GA 30602, USA

[E]USDA Forest Service, Pacific Northwest Research Station, Pacific Wildland Fire Sciences Laboratory, 400 North 34th Street, Suite 201, Seattle, WA 98103, USA.

[F]Corresponding author: Email: ahudak@fs.fed.us

Surface fuel and fire radiative energy measures

Abstract

Small-scale experiments have demonstrated that fire radiative energy is linearly related to fuel combusted but such a relationship has not been shown at the landscape level of prescribed fires. This paper presents field and remotely sensed measures of prefire fuel loads, consumption, fire radiative energy density (FRED), and fire radiative power flux density (FRFD) from which FRED is integrated, across forested and nonforested RxCADRE 2011 and 2012 burn blocks. Airborne longwave infrared (LWIR) image time series were calibrated to FRFD and integrated to provide FRED. Surface fuel loads measured in clip sample plots were predicted across burn blocks from airborne lidar-derived metrics. Maps of surface fuels and FRED were corrected for occlusion of the radiometric signal by the overstory canopy in the forested blocks, and FRED maps were further corrected for temporal and spatial undersampling of FRFD. Fuel consumption predicted from FRED derived from both airborne LWIR imagery and various ground validation sensors approached a linear relationship with observed fuel consumption, which conforms to theory. These field, airborne lidar and LWIR image datasets, both before and after calibrations and corrections have been applied, will be made publicly available from a permanent archive for further analysis and to facilitate fire modeling.

Summary

We present ground-based and remotely-sensed data used to predict surface fuel loads and fire radiative energy density (FRED) from the 2011 and 2012 RxCADRE prescribed fires. Relationships between observed and predicted surface fuel loads, and fuel consumption observed and predicted from FRED, approach linearity as expected by theory.

Surface fuel and fire radiative energy measures

Introduction

The physical process of vegetation biomass burning greatly influences terrestrial ecosystem structure and function, at spatial scales ranging from forest, savanna, and grassland biomes where fires affect the Earth system (Seiler and Crutzen 1980; Bowman *et al.* 2009) to the landscape level where humans apply prescribed fires and other vegetation management decisions (Lavorel *et al.* 2007; Trigg and Roy 2007). Prior remote sensing investigations to measure biomass burning rates likewise range broadly in scale, from coarse spatial resolution global monitoring satellites (Roberts and Wooster 2008) to airborne thermal imaging platforms (Riggan *et al.* 2004) with high resolution more suited for monitoring individual wildfires.

Geostationary satellites such as Meteosat bearing the Spinning Enhanced Visible and Infrared Imager (SEVIRI) sensor (Wooster *et al.* 2005; Roberts and Wooster 2008; Wooster *et al.* 2013) have coarse spatial resolution (3 km) but are well suited for regional-global scale studies of combusted biomass derived from estimates of total fire radiative energy (FRE) measured in joules (J), which are integrated over time from repeated measures of fire radiative power (FRP) measured in watts (J s^{-1}). The polar-orbiting Terra and Aqua satellites bearing the MODIS sensor, on the other hand, have higher spatial resolution (1 km) yet provide FRP measures only twice daily at best (Roberts *et al.* 2011) and therefore require fusion with burn area maps or other approaches to estimate FRE (Boschetti and Roy 2009; Freeborn *et al.* 2010; Kumar *et al.* 2011). Dickinson *et al.* (this issue) provide more details on active fire detection and FRP estimation from MODIS as well as VIIRS imagery from which both 750-m and 375-m resolution active fire products are derived (Schroeder *et al.* 2014).

Wooster *et al.* (2005) demonstrated in small-scale burning experiments that FRP is linearly related to biomass combustion rate, and that FRE is linearly related to biomass combusted (see also Freeborn et al. 2010 and Kremens et al. 2012). The latter quantity represents a greater measurement challenge because it requires sufficient sampling over time to integrate FRE from instantaneous measures of FRP. Temporal sampling resolution of active fire by fixed-wing aircraft is limited to 2 to 3 minutes, the rate at which the same airspace can be revisited. Riggan *et al.* (2004) used airborne active fire imagery to estimate carbon and energy fluxes from individual fires in Brazil. However, integration of total FRE from airborne FRP image time series collected over the entire duration and spatial extent of a fire has not yet been achieved.

Still also to be achieved is the prediction of surface fuel loads, including those beneath a forest canopy, using the canopy-penetrating and three-dimensional capability of airborne lidar. Canopy fuel parameters used in fire behavior modeling, namely crown bulk density, have been predicted from airborne lidar in coniferous forests (Riaño *et al.* 2003; Riaño and Chuvieco 2004; Andersen *et al.* 2005). Seielstad and Queen (2003) described the potential of airborne lidar for differentiating between surface fuel models in lodgepole pine forests. Terrestrial lidar has been used to classify surface fuel types within high-resolution fuel cells in fire-maintained longleaf pine forests (Hiers *et al.* 2009; Loudermilk *et al.* 2009, 2012), while Rowell and Seielstad (this issue) show that terrestrial lidar can be used in concert with an airborne lidar-derived digital terrain model (DTM) to characterize surface fuel heights at high resolution. However, surface fuel loads as exist beneath the longleaf pine forests occurring at Eglin Air Force Base in Florida, the site of these RxCADRE prescribed fires, have not been predicted as a continuous variable from airborne lidar.

The primary objective in this paper was to predict fuel consumption from estimates of FRE replicated at the landscape level of entire burn blocks. Attaining this objective compelled us to pursue the preliminary objective of predicting surface fuel loads and fuel combusted across these same burn blocks. Our chosen blocks were burned with prescribed fires at Eglin Air Force Base (AFB) in 2011 and 2012 as part of the RxCADRE project and imaged by both the Wildfire Airborne Sensor Platform (WASP) long-wave infrared (LWIR) sensor and a scanning lidar sensor mounted aboard the same aircraft.

Methods

Prescribed burn blocks

This paper considers the prescribed RxCADRE fires conducted at Eglin Air Force Base in 2011 and 2012. The two 2011 burns of forested blocks 703C and 608A were ignited by delayed aerial ignition devices dispensed from a helicopter. The nine blocks burned on the B70 range in 2012 were lit with drip torches on the upwind side to produce a more natural fireline progression through the blocks. One large block (L2F) was forest dominated by longleaf pine (*Pinus palustris* Mill.), while the other two large blocks (L1G and L2G) and six small blocks (S3, S4, S5, S7, S8 and S9) were nonforest. Surface fuels were composed of variable proportions of grasses, forbs, and shrubs dominated by turkey oak (*Quercus cerris* L.). Further details regarding the prescribed fires may be found in the overview paper by Ottmar *et al.* (this issue).

Ground measures

Surface fuel loads were measured by destructive harvesting in 1-m x 1-m clip plots within all burn blocks except L2F, where clip plots were 0.5-m x 0.5-m. The pre- and postfire clip plot positions alternated across a given sample unit, hence consumption could not be estimated at the plot level (i.e. consumption estimates were limited in resolution to the sample unit level). A sample unit consisted of a set of clip plots arranged systematically in one of three configurations:

(1) surrounding a 40-m x 40-m (2011) or 20-m x 20-m (2012) highly-instrumented plot (HIP) that was randomly located within a representative fuel condition inside a large burn block (with 2 to 3 HIPs per large burn block); (2) surrounding a 200-m x 100-m small burn block; or (3) along parallel transects from a random starting point within a large burn block. Details on the fuel sampling protocols can be found in Ottmar *et al.* (this issue).

Various ground sensors were deployed to collect voltage data calibrated to fire radiative power flux density (FRFD) time series that were subsequently integrated over time to provide independent measures of fire radiative energy density (FRED) for this analysis. Radiometers and infrared (IR) cameras were usually deployed inside a HIP. O'Brien *et al.* (this issue) provide sensor specifications of IR cameras, which were either nadir-viewing deployed on a 8.2-m tripod within the large burn block HIPs in 2011 and 2012 and within the small burn blocks in 2012, or oblique-viewing and deployed on a 26-m boom lift parked outside the fire perimeter for a synoptic view of the six small burn blocks (O'Brien *et al.*, this issue). Dickinson *et al.* (this issue) provide sensor specifications on dual-band "pocket" radiometers. Dual-band "pocket" radiometers deployed by Dickinson *et al.* differed from "orange box" radiometers used by O'Brien *et al.* in their field of view and bandpass, but both types of radiometers upon instrument-specific calibrations provided FRFD outputs which, upon time integration, yielded estimates of average FRED over their fields of view.

Airborne lidar

Airborne discrete-return lidar data were collected by Kucera International using a Leica ALS60 sensor on 5 February 2011 (703C), 6 February 2011 (608A), and 3 November 2012 (B70 burn blocks). Vertical uncertainty quantified with root mean squared error (RMSE), comparing the laser-measured ground heights to independent ground control points (GCPs) geolocated with a resource-grade global positioning system (GPS, Trimble Pathfinder ProXT), was 0.600 m at 703C (n = 9 GCPs) and 0.642 m at 608A (n = 12 GCPs) in 2011. In 2012, installation of survey-grade GCPs (n=20) reduced the vertical uncertainty by almost an order of magnitude (RMSE = 0.082 m). However, average vertical bias was comparable between all three lidar collections (-0.010 m at 703C, 0.003 m at 608A, 0.007 m at B70), as were the flight and lidar sensor operation parameters (Table 1). Terrascan software was used to classify and edit the lidar data.

A 1-meter DTM was interpolated from the vendor-classified ground returns using the GridSurfaceCreate function of FUSION (McGaughey 2014). The ‘minimum’ switch was used rather than the default ‘mean’, such that the DTM took the value of the minimum point height in each grid cell, as the intention was to minimize the number of near-ground returns with negative heights.

The ClipData function of FUSION was used to clip points within a 3-m radius of clip plot center coordinates. The ‘height’ switch was used in conjunction with the DTM to normalize absolute point heights to relative heights above ground. Using the CloudMetrics function of FUSION, canopy height and density metrics were calculated from lidar returns between 0 and 2 m above ground and within a 3-m radius of each prefire clip plot. The metrics included height distributional statistics calculated across the 0 to 2 m height range, as well as within vertical strata of 0–0.05, 0.05–0.15, 0.15–0.50, 0.50–1.0, and 1.0–2.0 m (Table 2).

The plot-level lidar metrics were considered as candidate predictor variables in a multiple linear regression model. The response variable, prefire surface fuel load, was natural log-transformed to produce a normal distribution. Best subsets regression was used to select the best predictors from the candidate predictor variables (Table 2), and minimizing the AIC statistic was the criterion used to choose the best subset model, following the approach of Hudak *et al.* (2006). The FUSION GridMetrics function was used to create gridded rasters of selected metrics at 5-m resolution for mapping. Overstory canopy cover was calculated as the number of first returns above a height threshold of 1.37 m (breast height) divided by the total number of returns, providing a physical measure of canopy cover (Smith *et al.* 2010). The canopy cover metric was calculated across the full extent of the lidar collections with the same origin, extent, and resolution as the gridded surface fuel metrics. The canopy cover grids were used to correct mapped surface fuel predictions upwards in the three forested blocks (703C, 608a, L2F) in proportion to overstory canopy cover.

Airborne LWIR imagery

The airborne WASP LWIR sensor imaged the active fires within the five large burn blocks. WASP has a nominal 8- to 9.2-m bandwidth (for further details see Dickinson *et al.*, this issue). Image frames were collected at 3- or 4-s intervals (Table 3). Using the ArcPy package in Python, raw WASP LWIR digital numbers were calibrated first to sensor-reaching radiance, L_{LWIR}, in W m^{-2} sr^{-1} in the passband of the WASP LWIR detector (Eqn. 1), and then to ground-leaving excitance, or observed FRFD ($FRFD_{obs}$) in W m^{-2} (Eqn. 2) as follows:

$$L_{LWIR} = f(DN) = 2 \times 10^{-6} DN^2 + 0.0176 DN \qquad (1)$$

$$FRFD_{obs} = \pi b\big(f(DN)\big)^M \qquad (2)$$

where *DN* is digital number, and *b* and *M* vary by WASP LWIR acquisition (Table 3) because of variable atmospheric absorption that was simulated with MODTRAN (Berk *et al.* 2003) based on temperature and humidity data recorded during the burns. These data along with further details regarding WASP LWIR image calibration are described in Accessory Publication 1 associated with Dickinson *et al.* (this issue). Calibrated image frames were resampled (nearest neighbor) and assembled into a multi-layer stack with a common origin, extent, and resolution based on the nominal resolution of the image frames (Table 3).

FRED in J m^{-2} was calculated from image time series of calibrated FRFD in W m^{-2}. Fire pixels were separated from nonfire pixels using a threshold of 1070 W m^{-2} derived independently from pocket radiometer data. The threshold can be thought of as the postfire FRFD value asymptotically approached by a pixel as it cools after burnover, making it greater than the apparent FRFD of unburned (background) pixels masked from consideration. To estimate the threshold, the peak FRFD was determined from all pocket radiometer datasets from 2012. For each dataset, FRFD measurements from before the peak were removed and the time rescaled so that peak time was assigned a value of t = 0. Then, parameters of a negative exponential model with an offset (the threshold) were fit to the individual datasets and the average threshold and its confidence interval determined from the results. The threshold was determined to be 1070 W m^{-2}, with no significant difference between radiometers in the forested versus nonforested blocks. Observed FRED ($FRED_{obs}$) calculated in J m^{-2} at each fire pixel, defined as having a minimum of one FRFD observation >1070 W m^{-2}, was calculated by Eqn. 3 as follows:

$$FRED_{obs} = \sum_{i}^{n} 0.5(FRFD_i + FRFD_{i-1})(t_i - t_{i-1}) \quad (3)$$

where $FRFD_i$ is pixel-level *FRFD* from each image *i* in the time series, and *t* is time in seconds (s). If pixel vectors only contained one FRFD measurement, then FRED was calculated by multiplying the single FRFD measurement by the sampling interval of either three (2012) or four (2011) seconds, depending on which burn block (Table 3).

Corrections for sampling biases

Surface fuel and fire radiative energy measures

Back-transformation of the surface fuel model predictions from the natural log (ln) scale to the natural scale introduced bias. This bias was corrected based on the mean square error (MSE) of the model residuals by Eqn. 4, following Baskerville (1972):

$$c_b = \exp^{(0.5\mathrm{MSE})} \tag{4}$$

Therefore, predicted fuels after back-transformation were multiplied by c_b.

A source of bias in both observed and predicted fuel loads was the exclusion of duff at the L2F block. Duff load was not measured at any RxCADRE burns except L2F and was therefore excluded from the fuel loads reported by Ottmar *et al.* (this issue). However, duff load was measured at L2F because substantial duff was evident in the field given that it had not burned for three years, longer than the other 2012 or 2011 burn blocks. Therefore, the prefire fuel load was increased by dividing the measured postfire duff load by the percentage consumption observed across the other fuel types (herbaceous, shrub, litter, woody), then adding the quotient to the measured prefire fuel load. Duff consumption was similarly increased under the assumption that the same proportion of duff was consumed as was observed across the other fuel types. These duff corrections were applied to both observations (field-based) and predictions (lidar-based) of surface fuel load and consumption.

Both the lidar-derived surface fuel maps and the WASP LWIR-derived FRED maps were affected by occlusion of the radiometric signal by the overstory canopy in the forested blocks. Canopy cover corrections were assumed to affect the airborne lidar signal and the LWIR radiation signal equally. Canopy-corrected fuel ($Fuel_{cc}$) and FRED ($FRED_{cc}$) were calculated at the pixel level by Eqns. 5 and 6, respectively:

$$Fuel_{cc} = Fuel_{pre}(1 + c_c) \tag{5}$$

$$FRED_{cc} = FRED_{obs}(1 + c_c) \tag{6}$$

where $Fuel_{pre}$ is predicted fuel and $FRED_{obs}$ is observed FRED (from Eqn. 3); c_c is the mapped canopy cover proportion.

The time that WASP LWIR was imaging the fire was much less than the time required for the aircraft to return to the airspace above the fire between passes. This temporal undersampling caused FRED to be underestimated. Therefore, the proportion of time that WASP LWIR was not actively imaging the burn block was calculated, as a correction for temporal undersampling bias.

The spatial extent (and resolution) of the WASP LWIR image frames depended on the flying height of the aircraft. Usually, only part of a large burn block was imaged within each WASP LWIR frame. Such spatial undersampling missed fire activity outside the image frame, especially in the larger burn blocks such as 608A; this resulted in FRFD and FRED being underestimated upon aggregation to the extent of the entire burn block. Therefore, the proportion of the burn block not imaged in each WASP LWIR frame was calculated and averaged across all frames as a correction for spatial undersampling bias.

The correction factors for temporal and spatial undersampling bias by WASP LWIR were assumed to be additive, as applied in Eqn. 7 to calculate a corrected FRED ($FRED_{cor}$):

$$FRED_{cor} = FRED(1 + c_t + c_s) \tag{7}$$

where $FRED$ is observed FRED ($FRED_{obs}$) averaged across the burn block either with canopy cover correction ($FRED_{cc}$) by Eqn. 6 (forest blocks) or without (nonforest blocks); c_t is temporal undersampling proportion, and c_s is spatial undersampling proportion.

Predicting fuel consumption from FRED

Predicting fuel consumption from FRED estimates derived from the ground-based IR cameras and dual-band radiometers required estimates of fire radiated fraction and an assumption of fuelbed heat of consumption. Kremens *et al.* (2012) estimated fire radiated fraction from 8-m x 8-m experimental burn plots in mixed-oak fuelbeds; the experimental plot fuels included additions of milled woody fuels and resulted in a large range in fuel consumption (0.2–3.2 kg m^{-2}). Predicted fuel consumption (FC_{pre}) was calculated following Reid and Robertson (2012) by Eqn. 8 as follows:

$$FC_{pre} = FRED / rf / hc \tag{8}$$

where $FRED$ is either FRED derived from the various IR validation sensors deployed on the ground or $FRED_{cor}$ derived from WASP LWIR after applying corrections (Eqns. 6,7); rf is fire radiative fraction (0.13–0.22) as estimated by Kremens *et al.* (2012) in similar mixed-oak fuelbeds; and hc is heat of combustion, which is a constant of 17.552 MJ kg^{-1} and includes ash, as reported by Reid and Robertson (2012), working in natural longleaf pine savanna and old field fuelbeds, where the heat of combustion is of similar magnitude.

Results

Surface fuel load

A prefire duff load of 1.94 Mg/ha at L2F was estimated by dividing the measured postfire duff load of 1.14 Mg/ha by the observed proportion consumed at L2F (0.5887) (Table 4). Estimating and adding duff load and consumption in L2F translated to a 21.9% increase above the prefire surface fuel load and a 26.3% increase above the consumption reported by Ottmar *et al.* (this issue) (Table 4).

Nine lidar metrics were selected as significant predictors in the best subsets, multiple linear regression model used to predict surface fuel loads (Table 5). The model explained 45% of the variance in ln-transformed surface fuel load and was highly significant (Table 5). The MSE of the residuals was 0.32, which when substituted into Eqn. 1, yielded a bias correction factor of 1.17 that was multiplied with the back-transformed predictions. Fig. 1 illustrates the equivalence plot (Robinson *et al.* 2005) of a simple linear regression model of the observed fuel loads at the 354 field plots regressed on the back-transformed, bias-corrected predictions; the model explains 32% of variation ($R^2 = 0.32$) and is highly significant ($p<0.0001$). Fig. 2 illustrates predicted surface fuel loads and fuel consumption (calculated from observed relative consumption, Table 4), with the higher fuel loadings and consumption existing in the forested blocks, particularly L2F, as was observed in the field. Surface fuel loads in L2F had accumulated for three years, for 2-3 years in L2G, for two years in 703C and 608A, and for one year in L1G.

The range of fuel predictions was not as broad as the range of fuel observations made on the ground (Fig. 1). This is a consequence of the regression modeling approach, which tends to compress the distribution of predictions toward the mean. However, fuel load and consumption predictions when aggregated to the block level compare favorably with observations, especially after correcting for canopy cover occlusion in the three forested blocks (Figs. 2, 3) and including the duff component in the L2F block (Fig. 3). Percentage canopy cover calculated from the airborne lidar returns above breast height (mean = 44%, s.d. = 20%) compared well with field measures of overstory canopy closure (mean = 43%, s.d. = 22%) collected prefire at the L2F clip plots (n = 60) using a spherical densiometer held at breast height (Pearson correlation = 0.60, p-value <0.0001). Since the gridded lidar measures of canopy cover (Table 4) were based on many orders of magnitude more data collected across the entire burn blocks, they were used to correct the surface fuel maps for canopy occlusion in a spatially-explicit manner (Fig. 2).

Fire Radiative Energy Density (FRED)

Correcting the FRED maps for overstory occlusion in the forested blocks using canopy cover calculated from the overstory lidar returns within the mapped FRED pixels increased FRED by the same proportions in the forest blocks as it did the maps of surface fuels (Fig. 2).

The parallel firelines apparent in the FRED images of the large burn blocks are an artifact of temporal undersampling (Fig. 4). The blue voids between the apparent firelines are typically not actual voids in surface fuel loads but “blind spots” where the aircraft was outside the airspace above the burn block when flame fronts spread through them (Fig. 4). They are most apparent in the L1G block where fuel loads were lightest (Ottmar *et al.* this issue) and the fire residence time and cooling period in a given pixel was least (O’Brien *et al.* this issue). The opposite extreme can be observed in the apparent lack of firelines throughout much of the L2F block, where surface fuel loads were heaviest and fire residence times and cooling periods were longest (Fig. 4). In the 703C and 608A blocks, patterns of FRFD (not shown) and FRED (Fig. 4) reflect numerous, simultaneous aerial ignitions from a helicopter.

Spatial undersampling was a smaller source of bias than temporal undersampling in the 2012 burn blocks but was a larger source for the especially large 608A block burned in 2011 (Table 3). Because the aircraft pilot sought to maximize coverage of the fire with each pass, the center of the burn blocks was more frequently imaged than some of the edges parallel to the flight path.

The more localized effect of the moving fireline on FRFD sampling intervals is illustrated in Fig. 5, comparing imagery between airborne WASP LWIR and nadir-viewing IR cameras deployed on the ground. The nadir IR cameras located within the HIPs imaged a restricted but fixed field of view continuously at 1- to 6-s intervals (depending on camera used). Thus, the data are not temporally undersampled like WASP LWIR. For instance, of the ten HIPs with coincident nadir IR camera and WASP LWIR measures of FRFD, WASP LWIR captured peak FRFD only twice (608A HIP SE, L1G HIP 2) (Fig. 5).

Relationship between fuel consumption and FRED

Thermal radiation sensors on the ground provided a means to validate the estimates of FRED generated from WASP LWIR, but without temporal and spatial undersampling. Predictions of fuel consumption based on ground observations of FRED facilitated more direct comparison between sensor types by whether predictions and observations deviated from a 1:1 relationship (Fig. 6). The pocket radiometers yielded the least biased predictions, suggesting that the radiative fraction at the RxCADRE burns was well-balanced between the minimum and maximum radiative fractions estimated by Kremens *et al.* (2012) in similar type fuels, also using dual-band pocket radiometers. Compared to observed consumption, consumption was under-predicted based on FRED derived from the orange box radiometers and nadir and oblique IR cameras deployed on the ground, and most of all from the WASP LWIR imagery (Fig. 6).

Discussion

To our knowledge, this paper is the first to predict surface fuel loads from airborne lidar metrics, including under forest canopies (Figs. 1-3), although the 5-m resolution of these maps is likely coarser than optimal to drive fire behavior models. Terrestrial lidar has been used to characterize surface fuel cells beneath longleaf pine canopies at the finer (<1 m) scales that drive fire behavior (Hiers *et al.* 2009; Loudermilk *et al.* 2009, 2012). Attempts to predict fine fuel loads from terrestrial lidar also are challenged by occlusion problems, but may be feasible from terrestrial lidar scanned obliquely from a boom lift (Rowell and Seielstad, this issue), like the oblique-viewing IR camera imagery of the small burn blocks (O'Brien et al., this issue) considered in this analysis.

Local accuracy in both the maps of surface fuels predicted from lidar (Fig. 2) and maps of FRED observed by WASP LWIR (Fig. 4) was admittedly poor, as was indicated by messy scatterplots (not shown) between these response variables at the radiometer locations. This is not surprising, given the high heterogeneity in fuels within the 25-m^2 cells within which the lidar metrics were calculated (Hiers *et al.* 2009; Loudermilk *et al.* 2009, 2012), overstory canopy occlusion of the lidar and LWIR signals from the ground, and temporal and spatial undersampling by WASP LWIR. As such, we focused on aggregated block-level instead of spatially-explicit comparisons.

The relationships between observed fuel consumption and consumption predicted from FRED using Eqn. 8 approach linearity when compared across burn blocks and sensor types (Fig. 6), and thus corroborate the 1:1 relationship between biomass combusted and FRE as found by Wooster *et al.* (2005) on small-scale experimental fires. Fuel consumption predicted from WASP LWIR was more biased than consumption predicted from all ground-deployed LWIR sensors, suggesting that FRED remains underpredicted despite our simplistic corrections for the cumulative biases caused by overstory canopy occlusion in the forest blocks and temporal and spatial undersampling in all large burn blocks (Eqns. 5–7).

Undersampling of FRFD over time and space accumulates into a more noticeable discrepancy in estimates of FRED upon integration (Fig. 6). Peak FRFD emittance is brief in these fine surface fuel conditions (Fig. 5), yet is typically much higher than mean FRFD in a highly skewed distribution; this nonlinearity of the FRFD response may contribute more to our apparent under-prediction of FRED than is accounted for by our simple corrections for temporal and spatial undersampling.

The proportion of the burn block where FRFD values >1070 W m^{-2} were never observed was also calculated as a third way to quantify fire activity that may have been missed. We did not correct for this third potential source of undersampling bias because it would seem to overestimate FRED, as if the ground were wholly covered by a continuous surface fuelbed. A large proportion of the ground cover in the burn blocks was exposed mineral soil devoid of fuel. In fact, mineral soil was ocularly estimated in 2012 before the fires at 30 distributed postfire clip plots per large burn block, and averaged 57.6% at L1G, 35.7% at L2G, and 15.7% at L2F, in inverse proportion to prefire litter cover, which averaged 35.0% at L1G, 49.3% at L2G, and 76.3% at L2F. These numbers reflect the time elapsed since previous burns: 1 year (L1G), 2-3 years (L2G), and 3 years (L2F). However, the continuity of the fuelbed was most conducive to fire spread in L2G among the large burn blocks, while the distribution of fuels in L1G would be best described as sparse, and in L2F as very patchy. Given the complex distribution of surface fuels both between and within burn blocks, we made no attempt to account for fuel heterogeneity in this first analysis. Furthermore, we did not attempt to account for variation in fuelbed components, but note here that consumption was dominated by the herbaceous component in the nonforest burn blocks and by the litter component in the forest blocks (Ottmar *et al.* this issue).

Conclusions

This study is the first to predict fine surface fuel loads from airborne lidar metrics at the landscape level of prescribed fires. It is also the first to integrate landscape-level estimates of FRED from FRFD observations derived from airborne LWIR image time series. Furthermore, fuel consumption predicted from FRED achieved near-linear relationships with observed consumption when compared across multiple sensor types and scales, as expected by theory. Future analyses will consider spatially-explicit corrections to these mapped variables. For instance, the fuels map might help to impute peak FRFD or FRED observations at the pixel level to fill in the sampling voids between apparent firelines, using either statistical or geostatistical interpolation methods. Such fuel maps may also serve as useful inputs into fire behavior models. Other datasets could also be integrated into future analyses, such as the terrestrial lidar data (Rowell and Seielstad, this issue) collected across the small burn blocks and at the large burn block HIPs. We intend to make the various raw, pre-processed and final field and map data products publicly available on the USFS Research Data Archive to facilitate new fire model development and further fundamental fire science research.

Acknowledgements

This research was funded primarily by the Joint Fire Science Program (Project #11-2-1-11) with additional support from the Strategic Environmental Research and Development Program (#RC-2243). We thank Kevin Hiers and Brett Williams for essential logistical support; Clint Wright, Bob Vihnanek, Joe Restaino, Jon Dvorak, Eva Strand and Donovan Birch for fuel sampling; and Kevin Satterberg for preparing data and metadata files for the RxCADRE data repository.

References

Andersen HE, McGaughey RJ, Reutebuch SE (2005) Estimating forest canopy fuel parameters using lidar data. *Remote Sensing of Environment* **94**, 441–229.

Baskerville GL (1972) Use of logarithmic regression in the estimation of plant biomass. *Canadian Journal of Forest Research* **2**, 49–53.

Berk A, Anderson GP, Acharya PK, Hoke M, Chetwynd J, Bernstein L, Shettle EP, Matthew MW, Alder-Golden SM (2003). MODTRAN4 version 3 revision 1 user's manual. Air Force Research Laboratory.

Boschetti L, Roy DP (2009) Strategies for the fusion of satellite fire radiative power with burned area data for fire radiative energy derivation. *Journal of Geophysical Research* **114**, D20302.

Bowman DMJS, Balch JK, Artaxo P, Bond WJ, Carlson JM, Cochrane MA, D'Antonio CM, DeFries RS, Doyle JC, Harrison SP, Johnston FH, Keeley JE, Krawchuk MA, Kull CA, Marston JB, Moritz MA, Prentice IC, Roos CI, Scott AC, Swetnam TW, van der Werf GR, Pyne SJ (2009) Fire in the earth system. *Science* **324**, 481–484.

Dickinson MB, Ellison L, Hudak AT, Ichoku C, Kremens RL, Loudermilk L, Hornsby B, O'Brien JJ, Paxton A, Schroeder W, Zajkowski T, Holley W, Bright B, Martinez O, Mauseri J (In Review) Comparing ground, airborne, and satellite measurements of fire radiative power – developing methods and datasets for cross-scale validation. *International Journal of Wildland Fire* (this issue).

Freeborn PH, Wooster MJ, Roberts G (2010) Addressing the spatiotemporal sampling design of MODIS to provide estimates of the fire radiative energy emitted from Africa. *Remote Sensing of Environment* **115**, 45–489.

Hiers JK, O'Brien JJ, Mitchell RJ, Grego JM, Loudermilk EL (2009) The wildland fuel cell concept: an approach to characterize fine-scale variation in fuels and fire in frequently burned longleaf pine forests. *International Journal of Wildland Fire* **18**, 315–325.

Hudak AT, Crookston NL, Evans JS, Falkowski MJ, Smith AMS, Gessler P, Morgan P (2006) Regression modeling and mapping of coniferous forest basal area and tree density from discrete-return lidar and multispectral satellite data. *Canadian Journal of Remote Sensing* **32**, 126–138.

Kremens RL, Dickinson MB, Bova AS (2012) Radiant flux density, energy density, and fuel consumption in mixed-oak forest surface fires. *International Journal of Wildland Fire* **21**, 722–730.

Kumar SS, Roy DP, Boschetti L, Kremens R (2011) Exploiting the power law distribution properties of satellite fire radiative power retrievals—a method to estimate fire radiative energy and biomass burned from sparse satellite observations. *Journal of Geophysical Research* **116**, D19303. doi: 10.1029/2011JD015676.

Lavorel S, Flannigan MD, Lambin EF, Scholes MC (2007) Vulnerability of land systems to fire: interactions among humans, climate, the atmosphere, and ecosystems. *Mitigation and Adaptation Strategies for Global Change* **12**, 33–53.

Loudermilk EL, O'Brien JJ, Mitchell RJ, Cropper WP, Hiers, JK, Grunwald S, Grego J, Fernandez-Diaz JC (2012) Linking complex forest fuel structure and fire behaviour at fine scales. *International Journal of Wildland Fire* **21**, 882–893.

Loudermilk EL, Hiers JK, O'Brien JJ, Mitchell RJ, Singhania A, Fernandez JC, Cropper WP, Slatton KC (2009) Ground-based LIDAR: a novel approach to quantify fine-scale fuelbed characteristics. *International Journal of Wildland Fire* **18**, 676–685.

McGaughey RJ (2014) FUSION/LDV: Software for LIDAR data analysis and visualization. Version 3.42. Seattle, WA: U.S. Department of Agriculture, Forest Service, Pacific Northwest Research Station. 179 p.

O'Brien JJ, Loudermilk L, Hornsby B, Hiers K, Ottmar R (in review) High resolution infrared thermography as a tool for capturing fire behavior in wildland fires. *International Journal of Wildland Fire* (this issue).

Ottmar RD, Hudak AT, Wright CS, Vihnanek RE, Restaino J (in review) Pre- and postfire surface fuel and cover measurements from experimental and operational prescribed fires in longleaf pine ecosystems of the southeast United States—RxCADRE. *International Journal of Wildland Fire* (this issue).

Ottmar RD, *et al.* (In Review) Datasets for fire model development and evaluation—the RxCADRE project. *International Journal of Wildland Fire* (this issue).

Reid AM, Robertson KM (2012) Energy content of common fuels in upland pine savannas of the south-eastern US and their application to fire behavior modelling. *International Journal of Wildland Fire* **21**, 591–595.

Riaño D, Meier E, Allgower B, Chuvieco E, Ustin SL (2003) Modeling airborne laser scanning data for the spatial generation of critical forest parameters in fire behavior modeling. *Remote Sensing of Environment* **86**, 177–186.

Riaño D, Chuvieco E (2004) Generation of crown bulk density for *Pinus sylvestris* from lidar. *Remote Sensing of Environment* **92**, 345–352.

Riggan PJ, Tissell RG, Lockwood RN, Brass JA, Pereira JAR, Miranda HS, Miranda AC, Campos T, Higgins RG (2004) Remote measurement of energy and carbon flux from wildfires in Brazil. *Ecological Applications* **14**, 855–872.

Roberts G, Wooster MJ (2008) Fire detection and fire characterization over Africa using Meteosat SEVIRI. *IEEE Transactions on Geoscience and Remote Sensing* **46**, 1200–1218.

Roberts G, Wooster MJ, Freeborn P, Xu W (2011) Integration of geostationary FRP and polar orbiter burned area datasets for an enhanced biomass burning inventory. *Remote Sensing of Environment* **115**, 2047–2061.

Robinson AP, Duursma RA, Marshall JD (2005) A regression-based equivalence test for model validation: Shifting the burden of proof. *Tree Physiology* **25**, 903–913.

Rowell EM, Seielstad CA (In Review) Developing and validating fuel height models for the RxCADRE experiments. *International Journal of Wildland Fire* (this issue).

Schroeder W, Oliva P, Giglio L, Csiszar I (2014) The new VIIRS 375 m active fire detection data product: algorithm description and initial assessment. *Remote Sensing of Environment* **143**, 85–96.

Seielstad CA, Queen L (2003) Using airborne laser altimetry to determine fuel models for estimating fire behavior. *Journal of Forestry* **101**, 10–15.

Seiler W, Crutzen PJ (1980) Estimates of gross and net fluxes of carbon between the biosphere and the atmosphere from biomass burning. *Climatic Change* **2**, 207-248.

Smith AMS, Falkowski MJ, Hudak AT, Evans JS, Robinson AP, Steele CM (2010) A cross-comparison of field, spectral, and lidar estimates of forest canopy cover. *Canadian Journal of Remote Sensing* **35**, 447–459.

Trigg SN, Roy DP (2007) A focus group study of factors that promote and constrain the use of satellite derived fire products by resource managers in southern Africa. *Journal of Environmental Management* **82**, 95–110.

Wooster MJ, Roberts G, Perry GLW, Kaufman YJ (2005) Retrieval of biomass combustion rates and totals from fire radiative power observations: FRP derivation and calibration relationships between biomass consumption and fire radiative energy release. *Journal of Geophysical Research-Atmospheres* **110**, D24311.

Wooster MJ, Roberts G, Smith AMS, Johnston J, Freeborn P, Amici S, Hudak AT. (2013) Thermal remote sensing of active fires and biomass burning events. pp. 347-390 In: Ch. 18, *Thermal Infrared Remote Sensing: Sensors, Methods, Applications* (C. Kuenzer and S. Dech, eds.), Remote Sensing and Digital Image Processing 17, Springer Dordrecht, 537 p. doi: 10.1007/978-94-007-6639-6_18.

Table 1. Parameters of airborne lidar collections prior to the 2011 and 2012 RxCADRE prescribed burns

Lidar collection parameter	2011	2012
Flying height above ground level	1200 m	1200 m
Sidelap	50%	50%
Field of view	24°	20°
Pulse rate	176.1 KHz	178.6 KHz
Average point density	4.5 points m^{-2}	5.5 points m^{-2}

Table 2. Lidar height and density metrics calculated from all returns between 0 m and 2 m above ground, and in six vertical sub-strata, within 3 m of clip plot center locations

These were the candidate lidar metrics considered for predicting surface fuel loads measured in prefire clip plots (n = 354).

Strata	Metrics
>0.0 and 2.0 m height	mean, mode, stddev, CV, skewness, kurtosis
>0.0 and <0.05 m height	mean, mode, stddev, CV, proportion
>0.05 and <0.15 m height	mean, mode, stddev, CV, proportion
>0.15 and <0.50 m height	mean, mode, stddev, CV, proportion
>0.50 and <1.0 m height	mean, mode, stddev, CV, proportion
>1.0 and <2.0 m height	mean, mode, stddev, CV, proportion

Table 3. Burn block names, burn dates, WASP LWIR calibration coefficients (power fit; Eqn. 3), sampling characteristics, and other attributes of the 2011 and 2012 RxCADRE prescribed burns at Eglin AFB

Temporal undersampling proportion is the proportion of time during which WASP was not imaging the burn block. Spatial undersampling proportion is the average proportion of the burn block not imaged in individual WASP frames.

Burn block	Burn date	b	M	WASP LWIR spatial resolution (m)	WASP LWIR sampling interval (s)	Temporally undersampled proportion	Spatially undersampled proportion
703C	6 February 2011	2.955	1.397	2.8	4	0.69	0.70
608A	8 February 2011	2.880	1.399	2	4	0.68	0.85
L1G	4 November 2012	4.158	1.412	3	3	0.76	0.63
L2G	10 November 2012	3.947	1.403	3	3	0.85	0.35
L2F	11 November 2012	3.753	1.409	1.5	3	0.85	0.68

Table 4. Burn block names, areas, and number of prefire clip plots used to predict surface fuels from airborne lidar metrics

Estimates of surface fuel load and consumption include estimates of duff load and consumption in the L2F burn block. The last column reports block-level means of the lidar-derived, overstory canopy cover grids used to correct maps of surface fuels (Fig. 2) and FRED (Fig. 4) in the forested blocks.

Burn block	Area (ha)	Clip plots included in fuel model (number)	Observed surface fuel load (Mg ha^{-1})	Observed absolute consumption (Mg ha^{-1})	Observed relative consumption (%)	Mean canopy cover proportion
703C	668	60	5.35	3.03	56.58	0.250
608A	828	40	5.97	4.68	79.12	0.227
L1G	454	57	2.15	1.54	72.66	0
L2G	127	57	3.57	3.09	85.33	0
L2F	151	65	10.80[1]	6.36[2]	58.87[3]	0.373
S3	2	0[4]	3.08	2.56	83.15	0
S4	2	0[4]	2.45	2.04	83.30	0
S5	2	0[4]	2.82	2.19	77.58	0
S7	2	25	4.11	1.80	43.82	0
S8	2	25	3.64	2.80	77.02	0
S9	2	25	2.42	1.40	57.76	0

[1]Fuel load reported by Ottmar *et al.* (this issue) (8.86 Mg ha^{-1}) was increased 21.9% to include duff.

[2]Consumption reported by Ottmar *et al.* (this issue) (5.03 Mg ha^{-1}) was increased 26.3% to include duff.

[3]Same percentage consumption as reported by Ottmar *et al.* (this issue); consistency was assumed when increasing the prefire fuel load and consumption to include duff.

[4]The S3, S4, and S5 blocks were burned on 1 November 2012, two days prior to the lidar survey; therefore, fuel measures at the 75 clip plots at these three blocks (see Fig. 2) were excluded from the predictive model, while the 75 clip plots at blocks S7, S8, and S9 (see Fig. 2) burned on 7 November 2012 were included.

Table 5. Multiple linear regression model predicting surface fuel loads (ln-transformed) from nine selected lidar metrics

Lidar predictor	Estimate	Std. Error	t value	Pr (>|t|)	Significance
(Intercept)	2.141	0.315	6.789	4.96e-11	***
Mean (0–2 m)	-1.767	0.780	-2.266	0.024	*
Kurtosis (0–2 m)	0.003	0.001	2.261	0.024	*
Mode (0–0.05 m)	-4.772	2.327	-2.051	0.041	*
Proportion (0–0.05 m)	-1.779	0.242	-7.355	1.41e-12	***
Proportion (0.05–0.15 m)	-1.777	0.308	-5.763	1.84e-08	***
Std Dev (0.05–0.15 m)	23.838	8.616	2.767	0.006	**
CV (0.15–0.50 m)	0.575	0.210	2.743	0.006	**
Std Dev (0.5–1m)	1.507	0.677	2.225	0.027	*
Std Dev (1–2m)	0.988	0.368	2.687	0.008	**
Model statistics:					
$R^2 = 0.456$; Adj. $R^2 = 0.442$	df = 344	RSE = 0.566	F = 32.07	p <0.0001	***

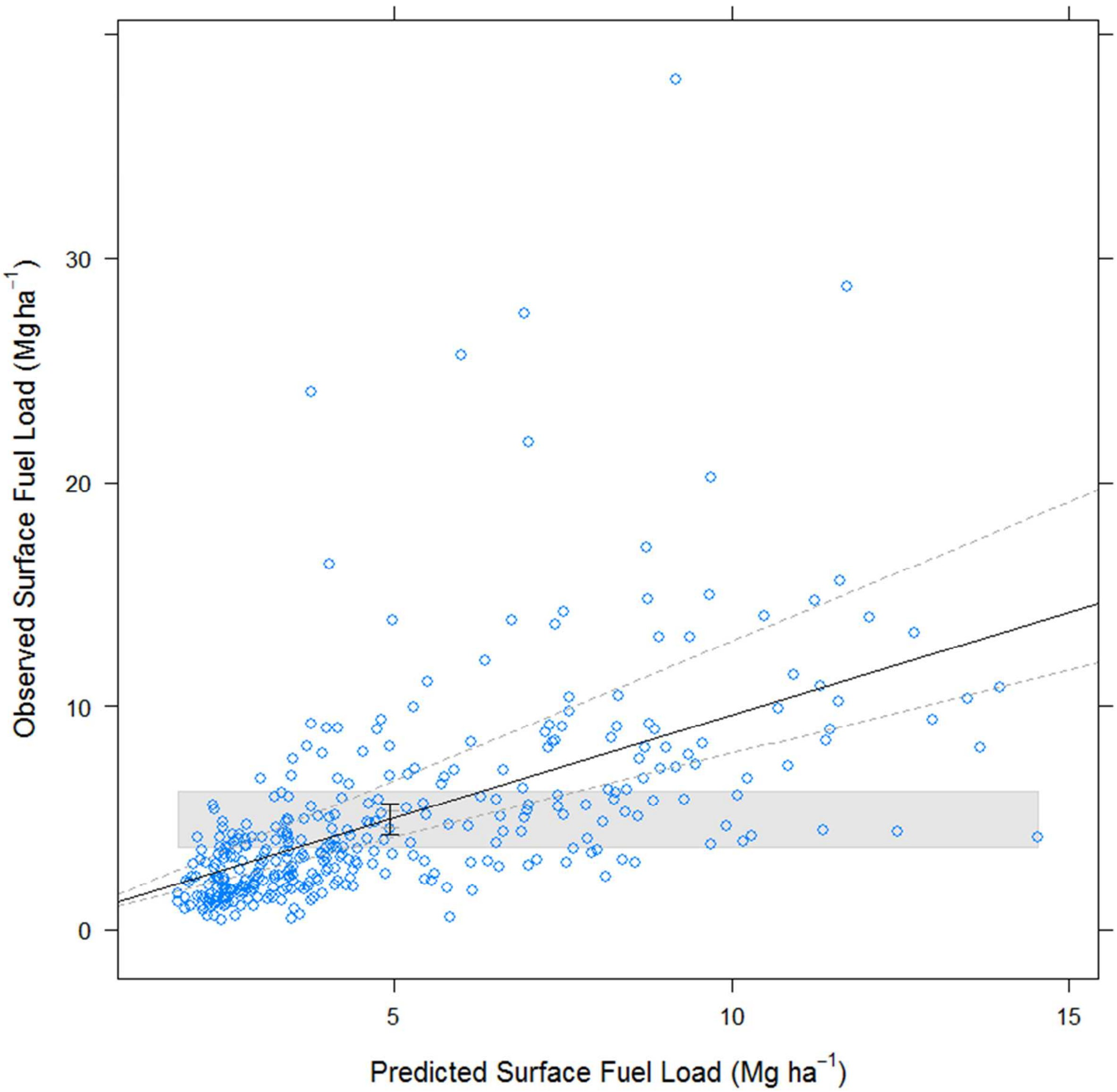

Fig. 1. Equivalence plot of predicted versus observed surface fuel loads after back-transformation to the natural scale and subsequent bias correction. The plot shows that the predictions are neither biased (error bars are within region of similarity defined by the gray shaded region) nor disproportional (regression line is within region of similarity defined by the diverging dotted lines) with respect to the observations.

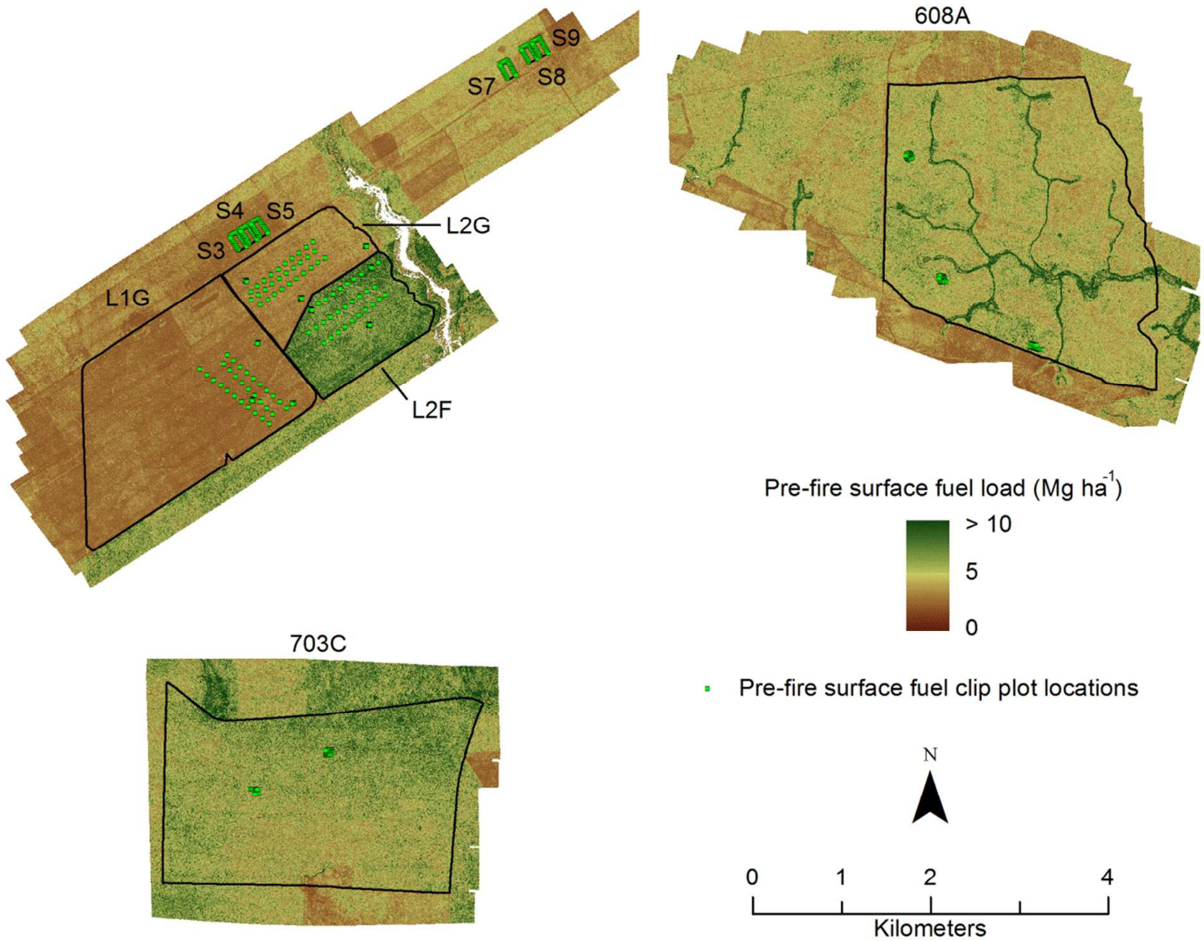

Fig. 2. Prefire surface fuels predicted across the extent of the 2011 and 2012 lidar collections. See Fig. 1, Ottmar *et al.* overview (this issue) for the locations of these burn blocks within Eglin AFB. Correction for overstory canopy occlusion in the forested areas has been applied.

Surface fuel and fire radiative energy measures

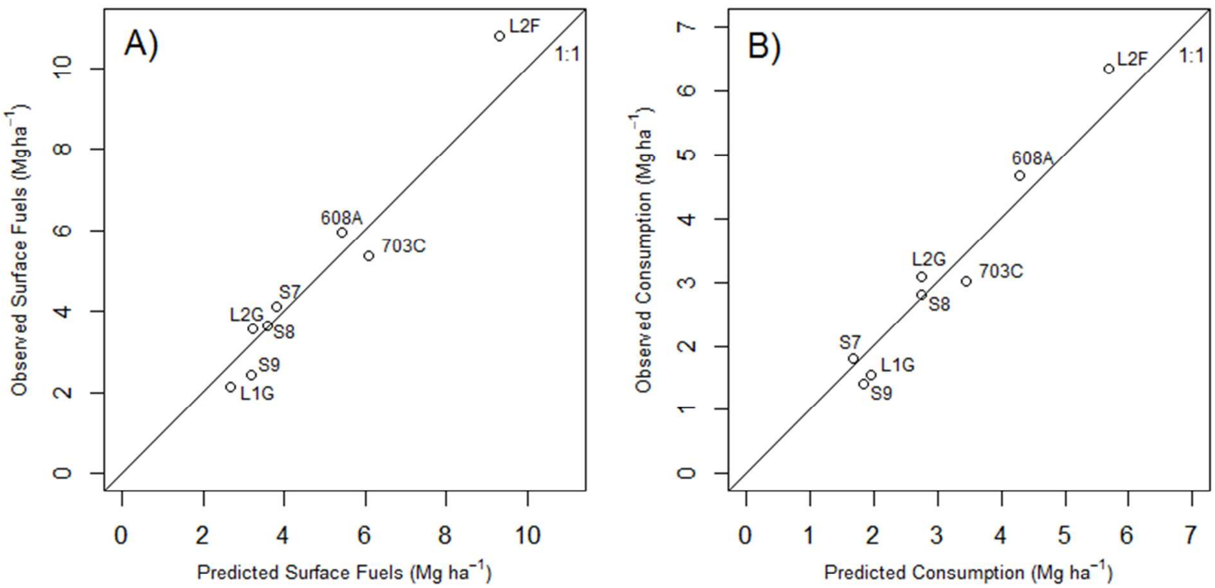

551

552 **Fig. 3**. Burn block-level comparisons between (A) surface fuels predicted from selected prefire
553 lidar metrics versus prefire surface fuels observed, and (B) consumption predicted (by
554 multiplying mean block-level surface fuels predicted in (A) by proportion consumed, Table 4)
555 versus consumption observed. Correction for overstory canopy occlusion in the forested blocks
556 has been applied to predictions in both graphs. Both observations and predictions have been
557 corrected for duff present in the L2F block.

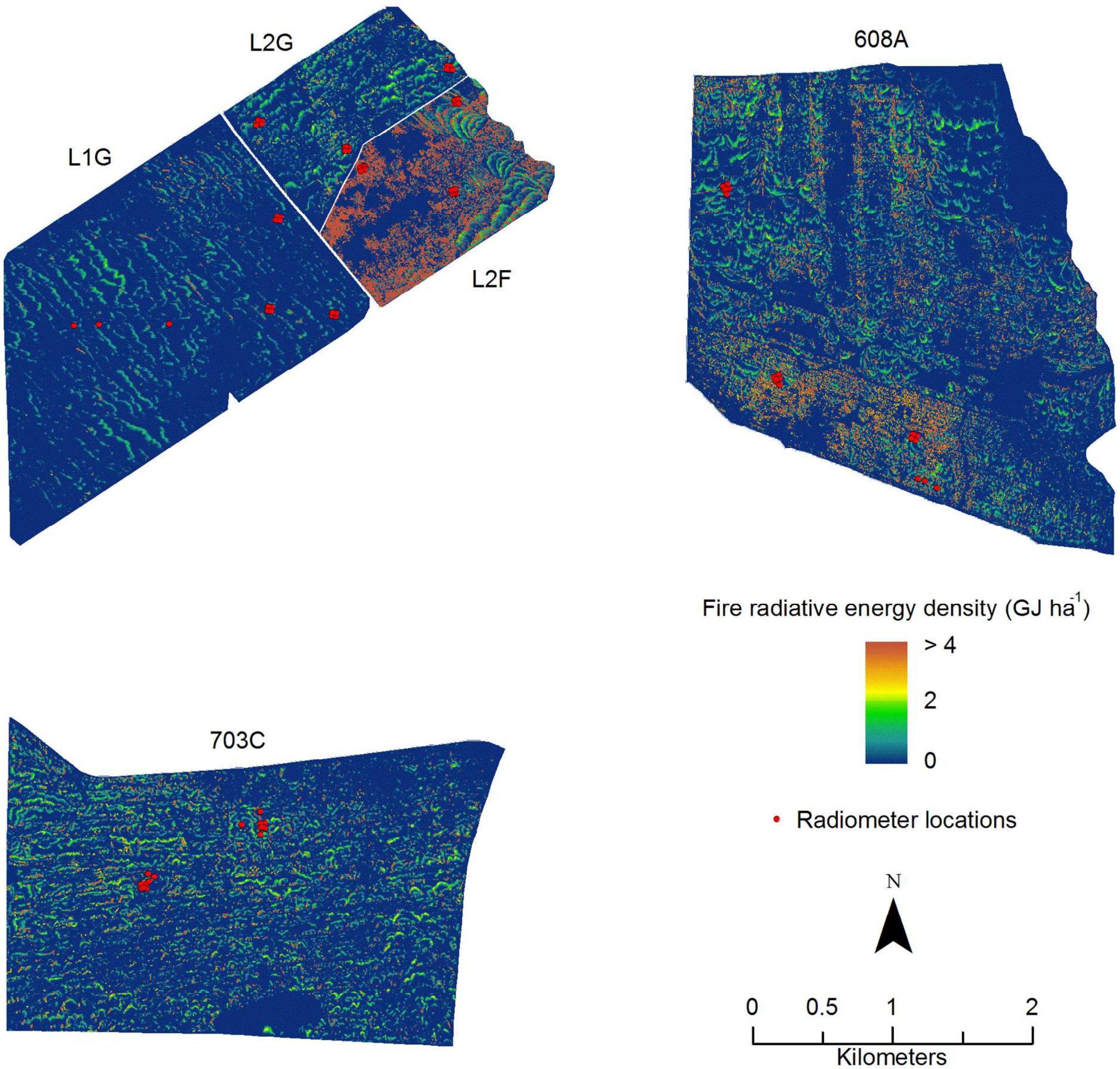

Fig. 4. FRED estimated from WASP LWIR-derived FRFD image time series collected across the extent of the 2011 and 2012 large burn blocks. See Fig. 1, Ottmar *et al.* overview (this issue) for the locations of these burn blocks within Eglin AFB. Correction for overstory canopy occlusion in the forested blocks has been applied.

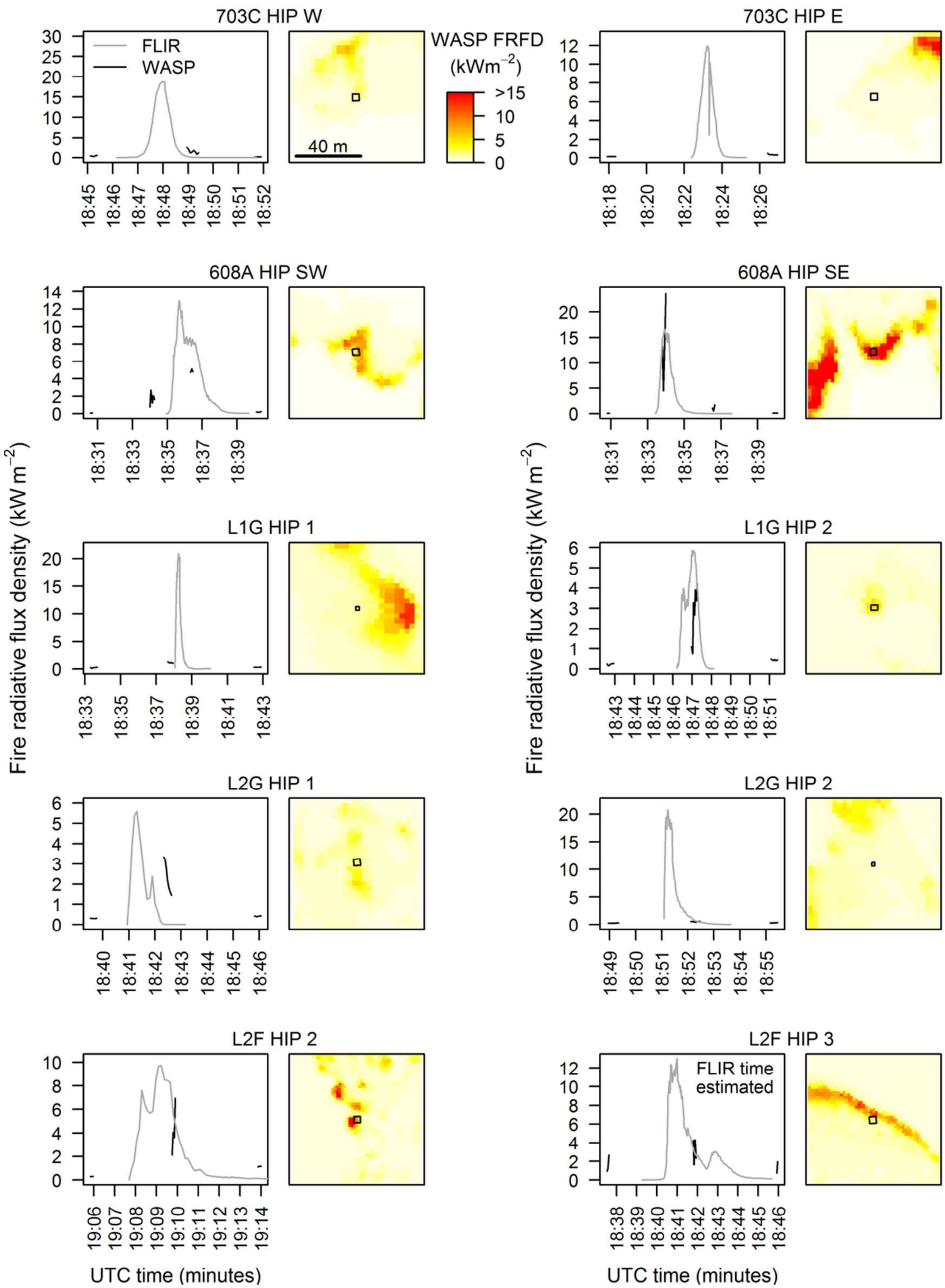

703C HIP W
FLIR
WASP
WASP FRFD
(kWm^{-2})
>15
10
5
0
40 m
703C HIP E
608A HIP SW
608A HIP SE
L1G HIP 1
L1G HIP 2
L2G HIP 1
L2G HIP 2
L2F HIP 2
L2F HIP 3
FLIR time
estimated
Fire radiative flux density (kW m^{-2})
UTC time (minutes)

Fig. 5. FRFD estimated at the scale of ten tripod-mounted, nadir-viewing IR cameras at the large burn block HIPs. The figure illustrates FRFD measured at two HIPs (columns) per each of the five large burn blocks (rows). Line graphs (on left of each pair) show the intermittent FRFD record obtained from WASP LWIR imagery compared to the FRFD recorded by the IR cameras as the flame front passed beneath. Heat images (on right of each pair) illustrate the closest position of the flame front to the IR camera field of view (tiny black box) as observed with WASP LWIR. The intention is to show temporal undersampling of WASP LWIR, which entirely missed the flame front in more cases than it captured peak FRFD at these fixed locations. (Note: Although the relative times recorded by the IR camera at L2F HIP 3 are accurate, the absolute times graphed are estimated because the start time failed to synchronize with UTC time.)

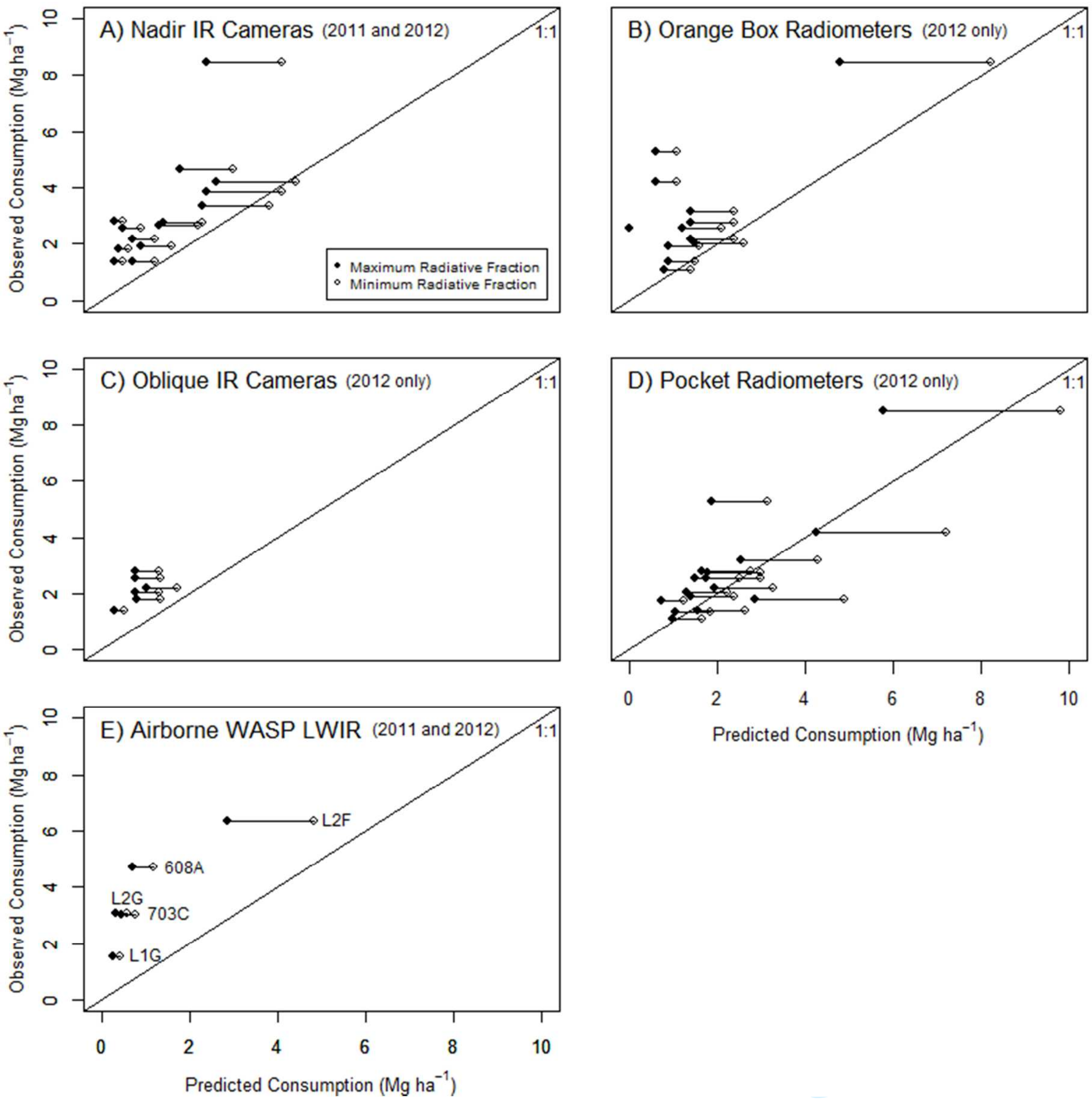

Fig. 6. Validation of fuel consumption predicted using Eqn. 8 (Reid and Robertson 2012) with FRED integrated from LWIR measures collected using five different sensor types: (A) tripod-mounted, nadir-viewing IR cameras (n = 14); (B) orange box radiometers (n = 12); (C) boom-mounted, oblique-viewing IR cameras (n = 6); (D) pocket radiometers (n = 60, aggregated to n = 16 sample units); and (E) airborne WASP LWIR imagery (n = 5), with all bias corrections applied. Horizontal line segments show expected ranges in predicted consumption based on

estimated maximum or minimum radiative fraction (Kremens *et al.* 2012), indicated respectively at the lower and upper ends of each segment. Observed consumption is derived from clip plot biomass samples.